PAPER • OPEN ACCESS

Epitaxy of boron nitride monolayers for graphene-based lateral heterostructures

2D Materials

PAPER

Epitaxy of boron nitride monolayers for graphene-based lateral heterostructures

James Wrigley[1], Jonathan Bradford[1] , Tyler James[1], Tin S Cheng[1], James Thomas[1], Christopher J Mellor[1], Andrei N Khlobystov[2], Laurence Eaves[1], C Thomas Foxon[1], Sergei V Novikov[1,*] and Peter H Beton[1,*]

1 School of Physics and Astronomy, University of Nottingham, Nottingham NG7 2RD, United Kingdom
2 School of Chemistry, University of Nottingham, Nottingham NG7 2RD, United Kingdom
* Author to whom any correspondence should be addressed.

E-mail: peter.beton@nottingham.ac.uk and sergei.novikov@nottingham.ac.uk

Abstract

Monolayers of hexagonal boron nitride (hBN) are grown on graphite substrates using high-temperature molecular beam epitaxy (HT-MBE). The hBN monolayers are observed to grow predominantly from step edges on the graphite surface and exhibit a strong dependence of the morphology, including the dominant crystallographic edge, of the hBN monolayers, on the growth temperature, as well as systematic variations in growth rate and coverage, and significant differences in the growth at monolayer and multilayer graphite steps. At graphite monolayer steps hBN grows laterally across the surface on the lower terrace, but hBN growth on the upper side of the graphite step is more limited and is nucleated by three-dimensional clusters. Multilayer graphite steps exhibit a much higher density of non-planar hBN aggregates and growth on both the upper and lower terraces occurs. The results show that the hBN monolayer growth edge type, hBN island shape and the presence of hBN aggregates can be controlled in HT-MBE, with the highest quality layers grown at a substrate temperature of about 1390 °C. Sequential HT-MBE growth of hBN, graphene (G) and a second cycle of hBN growth results in the formation of monolayer thick lateral hBN–G–hBN heterostructures, in which a strip of G is embedded between monolayers of hBN.

1. Introduction

There has been a surge of interest [1] in hexagonal boron nitride (hBN) due to its technological potential for deep ultraviolet (DUV) photonics [2, 3], single photon emitters [4], and through its incorporation into van der Waals (vdW) heterostructures [5] as either a substrate, tunnel barrier or capping layer. While the technological potential of hBN has attracted the attention of many leading international groups, high-quality hBN material has proved difficult to grow in either bulk form, or as thin films.

hBN exhibits many structural similarities with graphite, including the same honeycomb structure, vdW interlayer bonding and an in-plane lattice constant, which although larger than graphite, differs only by 1.8% [6]. Electronically, hBN is a large bandgap semiconductor, ∼6 eV [1, 2], in bulk, multilayer and monolayer form [7]. hBN is commonly used to encapsulate two-dimensional (2D) materials as a strategy to improve device performance, as its inert nature protects against degradation and contamination [8]. Due to the lack of dangling bonds and charge impurities hBN is also an excellent substrate for 2D materials, such as for the growth of graphene (G) [5]. However, large area hBN layers are difficult to reliably produce, a limitation on which progress has only recently been made.

Chemical vapor deposition (CVD) has become the primary low cost method for the growth of hBN layers. The growth has been explored on various transition metal substrates, as is common in CVD due to the associated catalytic nature at high temperatures. Similar to CVD-grown G, the most popular choices of substrate for monolayer hBN CVD growth are Cu(111) and Ni(111) due to the small lattice mismatches, which facilitate commensurate growth, and the low solubility of B and N [9–11]. Recent

studies have established the production of high quality and large scale growth of hBN on metallic substrates [11–16]. However, limitations remain, due to difficulties in retaining the quality of the grown hBN layers when transferring to standard semiconductor substrates for functioning devices. Rapid progress has been made in the production of hBN on non-metallic substrates, both with CVD [17] and mainly by metal-organic chemical vapour deposition [18–21].

To date there has been relatively little focus on the production of hBN by molecular beam epitaxy (MBE), but there are potential advantages to its development. In this process the substrate temperature, growth time, and deposition rate are controllable, with the potential to optimise and manipulate the resulting hBN interfacial quality and growth morphology. Multiple connected growth chambers configured with the requisite sources can be used to produce samples while maintaining a vacuum throughout the growth. Using MBE helps avoid the sample contamination issues that arise from the etching and layer transfers required for device fabrication by CVD [22]. The growth of hBN via MBE has been studied previously using a wide variety of substrates such as diamond(001) [23, 24], Ni(111) [25–28], cobalt [29–31], sapphire(0001) [32] and highly oriented pyrolytic graphite (HOPG) [7, 33–35], see Cheng *et al* 2018 and the references therein [33]. Graphite provides a good surface for hBN growth due to its low lattice mismatch, and isostructural similarity to hBN.

We have recently developed high-temperature MBE (HT-MBE) for the growth of hBN at temperatures from 1250 °C to 1700 °C [7, 33–36]. We have demonstrated that by growing hBN on HOPG substrates at these extremely high temperatures it is possible to produce monolayer and few-layer thick boron nitride with atomically flat surfaces, which are essential for future 2D and DUV applications. The hBN coverage can be reproducibly controlled by the growth time, substrate temperature and boron to nitrogen flux ratios. We have demonstrated that if the epitaxy temperature is decreased to under 1250 °C, the optical properties of the hBN layers degrade [33, 36].

In addition to the standard conventional hBN–G vertical heterostructures, recent studies have focused on the development of novel 2D lateral heterostructures. These lateral heterostructures consist of multiple connected monolayer thick materials within the same atomic plane. Recently, it has been shown in two review articles on the subject [37, 38], that many 2D devices fabricated with the use of lateral heterostructures can demonstrate superior performance or have novel and unique transport and optical properties. Lateral heterostructures can be successfully realised and are now actively studied not only in the hBN–G combination, but also in WSe_2–WS_2, MoS_2–$MoSe_2$ semiconductors and

many other 2D material systems [37, 38]. Lateral heterostructures have several potential advantages over vertically stacked 2D materials structures, such as eliminating the possibility of interlayer contamination [37, 39].

Theoretical modelling of G–hBN based lateral heterostructures was crucial for their rapid development, interface engineering of their electronic properties and prediction of their potential device applications [39–41], as described by Wang *et al* [37] and Wang *et al* [38] and other references therein. Theoretical modelling has proven effective in explaining band alignment of 2D hBN–G lateral heterostructures and the origin of epitaxial growth from zigzag and armchair edges [39, 41].

Whereas vertical 2D heterostructures can be produced by exfoliating and stacking 2D layers, lateral 2D heterostructures can only feasibly be produced by an epitaxial growth process. In this case, step edges on the surface act as nucleation sites for sequential monolayer growth and become the interfaces of the developed heterostructures. The main method for the growth of lateral hBN–G heterostructures so far is CVD [37, 38]. There are different approaches in the CVD growth of lateral heterostructures. In sequential CVD epitaxy of hBN and G monolayers, step-flow growth is a self-assembled process, where it is difficult to control the shape and size of the interface. In sequential CVD epitaxy, there is also a problem of thermal-induced degradation of the previously grown layers, due to different required epitaxial temperatures [37]. That has increased the interest in CVD of hBN–G heterostructures using a spatial control based on photolithography and etching techniques. For example, the G layer can be initially grown by CVD, then patterned with photolithography, the unwanted areas can be etched, followed by a second cycle of selective epitaxy of the hBN layer [37]. The direct selective chemical conversion of G layers to hBN stripes has also been explored using CVD, resulting in lateral hBN–G 2D heterostructures [37].

The properties of hBN–G lateral heterostructures are dependent on the interfaces and geometries of the alternating domains of hBN and G [39, 42]. Previous works in lateral heterostructures have employed G and hBN, aiming to obtain a tuneable band gap from the integrated hybrid monolayer or novel electronic and magnetic properties from domain interfaces [43–47]. Studies making use of CVD epitaxy have achieved some success [48–53], leading to the formation of atomically thin lateral devices [37, 54–56]. The lateral 2D hBN–G devices allow mono-atomically thin circuitry and at the same time are likely to remain mechanically flexible and optically transparent, allowing transfer to arbitrary substrates for flexible and transparent electronics [55]. For example, the first hBN–G 2D resonators and 2D field-effect transistors for flexible 2D optoelectronics have been reported [54].

Here we focus on utilising HT-MBE, a potentially scalable and clean epitaxial technique, to investigate the growth of hBN–G–hBN lateral heterostructures on graphite substrates. The hBN monolayers on graphite grown here were produced using a nitrogen plasma source coupled with an electron beam evaporator to provide a source for boron. The substrate temperature ranged from 1080 °C to 1520 °C, and the width of the resulting hBN epilayers growing from the graphite substrate steps, typically ranging from ∼30 to 150 nm, varies with growth time and substrate temperature. The G HT-MBE growth was achieved by the electron beam evaporation of high-purity graphite. Our earlier studies focus primarily on the DUV optical and electronic properties of the hBN monolayers [7, 33, 34, 36], whereas here the main emphasis will be placed on the HT-MBE control of the shape of hBN monolayer islands. Subsequent HT-MBE lateral growth of hBN, G and a final hBN monolayer, results in a monolayer-thick lateral hBN–G–hBN heterostructures.

2. Experimental

The growth of hBN and G layers was studied using a custom-designed dual chamber Veeco GENxplor MBE system, modified to achieve, in each chamber, substrate temperatures up to 1850 °C (measured using a thermocouple) under ultra-high vacuum (UHV) conditions on a rotating substrate [7, 33–36, 57, 58]. In one of the HT-MBE chambers, a standard Veeco RF plasma source is used to produce a flux of active nitrogen for the growth of hBN. All hBN layers investigated in this paper were grown using a fixed RF power of 550 W and a nitrogen flow rate of 2 sccm. In the same chamber there are two independent MBE sources for boron, a Veeco high-temperature effusion Knudsen cell and a vertical electron beam evaporator EBVV 63-T4, produced by Dr Eberl MBE Komponenten GmbH. Both sources are filled with high-purity (5 N) elemental boron, which contain a natural mixture of ^{11}B and ^{10}B isotopes. During hBN growth with the e-beam source, a current of 50 mA and accelerating voltage of 6 kV were used. Growth times of 20 mins, 40 mins, and 1 h resulted in hBN monolayer surface coverage up to, typically, 50% of the surface. Throughout growth the substrate was held at temperatures between 1080 °C and 1520 °C, as specified for each sample.

The growth of G layers was performed in a second HT-MBE chamber within the same UHV system. A similar vertical electron beam evaporator EBVV 63-T4 was fitted with a high-purity pyrolytic graphite charge as anode target to produce the carbon flux for G growth. Details of the G HT-MBE system can be found elsewhere [35, 57, 58]. During G growth the e-beam current was increased to, typically, 300 mA, with an accelerating voltage of 5 kV and the substrate temperature was estimated to be 1390 °C for all samples.

HOPG substrates (10 × 10 mm^2) with a mosaic spread of 0.4° were first cleaned by exfoliation using adhesive tape to obtain a fresh graphite surface for epitaxy. After exfoliation, the HOPG substrates were cleaned by immersion in toluene for 4 h, before heating to 400 °C for 8 h in a flowing (0.15 slpm) Ar/H$_2$ (95:5) atmosphere.
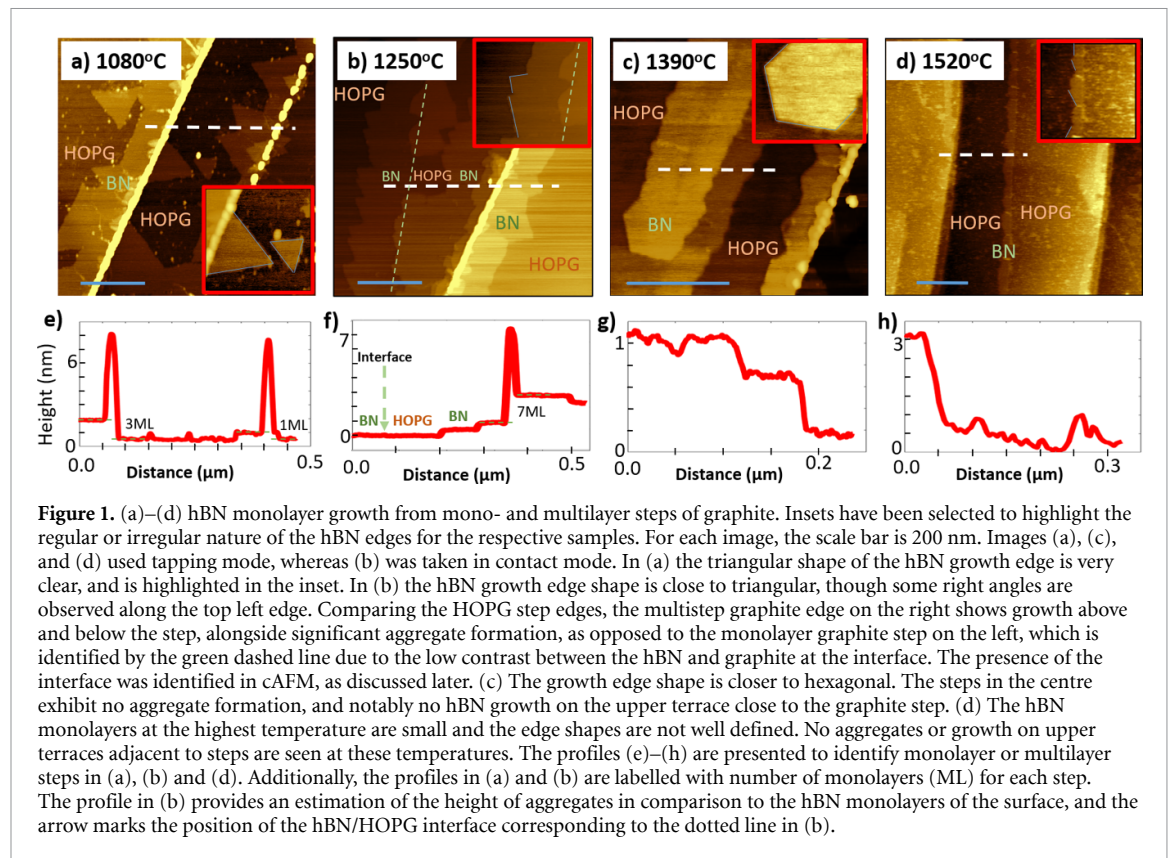
After HT-MBE growth the samples are removed from the system to allow the acquisition of atomic force microscopy (AFM) images of the surface. Tapping mode and conductive mode AFM images were acquired using an Asylum Research Cypher-S instrument with NuNano Scout 70, and Spark 70 Pt probes respectively. Distinguishing between materials is primarily achieved using the phase channel (tapping mode), and the conductive channel (conductive AFM). Conductive AFM current images were obtained by measuring current flow under an applied bias between tip and sample of −50 mV (the tip is earthed). All images were then processed with the Gwyddion software package [59].

Additionally, X-ray photoelectron spectroscopy (XPS) measurements were performed to establish the elemental composition of the grown material. The XPS measurements show that there are minimal contaminants in the systems; these results are presented in supplementary information (SI) (available online at stacks.iop.org/2DM/8/034001/mmedia).

3. Results

Figure 1 shows AFM images of samples following HT-MBE of hBN at substrate temperatures ranging from 1080 °C to 1520 °C with a growth time of 40 min. Several features are common to all samples. Firstly, hBN monolayers grow outward from step edges in the graphite and the monolayer width reduces as the temperature is raised, which can be observed from figures 1(a)–(d). Straddling the steps are amorphous aggregates of boron nitride, which appear in topographic AFM images as bright spots or lines, with a density which is reduced as the growth temperature is increased. Other key points in these AFM images, which will be discussed in greater detail below, are the differences in the shape of the hBN monolayer facets, and the presence of hBN monolayers on the upper and lower graphite terraces close to a HOPG step. In addition, there are pronounced differences between the growth of hBN nucleated at monolayer and multilayer graphite steps.

In figure 1(a) the sample grown at 1080 °C shows monolayer hBN islands with, predominantly, a triangular shape. The majority of the grown hBN is nucleated at HOPG step edges, but there are also hBN islands nucleated on the HOPG terraces. In figure 1(b), grown at higher temperature, a significant reduction in aggregate presence is observed at all

Figure 1. (a)–(d) hBN monolayer growth from mono- and multilayer steps of graphite. Insets have been selected to highlight the regular or irregular nature of the hBN edges for the respective samples. For each image, the scale bar is 200 nm. Images (a), (c), and (d) used tapping mode, whereas (b) was taken in contact mode. In (a) the triangular shape of the hBN growth edge is very clear, and is highlighted in the inset. In (b) the hBN growth edge shape is close to triangular, though some right angles are observed along the top left edge. Comparing the HOPG step edges, the multistep graphite edge on the right shows growth above and below the step, alongside significant aggregate formation, as opposed to the monolayer graphite step on the left, which is identified by the green dashed line due to the low contrast between the hBN and graphite at the interface. The presence of the interface was identified in cAFM, as discussed later. (c) The growth edge shape is closer to hexagonal. The steps in the centre exhibit no aggregate formation, and notably no hBN growth on the upper terrace close to the graphite step. (d) The hBN monolayers at the highest temperature are small and the edge shapes are not well defined. No aggregates or growth on upper terraces adjacent to steps are seen at these temperatures. The profiles (e)–(h) are presented to identify monolayer or multilayer steps in (a), (b) and (d). Additionally, the profiles in (a) and (b) are labelled with number of monolayers (ML) for each step. The profile in (b) provides an estimation of the height of aggregates in comparison to the hBN monolayers of the surface, and the arrow marks the position of the hBN/HOPG interface corresponding to the dotted line in (b).

hBN step terraces. Triangular facets evolve on many of the growing hBN islands, but there is very little nucleation on terraces (unlike figure 1(a)). A notable difference is observed in the growth and aggregate formation close to multilayer and monolayer HOPG steps; the monolayer graphite step, identified with the dashed line (and the arrow in figure 1(f)), exhibits almost no aggregate presence and hBN growth occurs predominantly on the lower terrace. Identification of the HOPG/hBN interface on the left of the image was carried out using conductive AFM (see SI). In contrast, the multilayer HOPG step on the right-hand side exhibits growth on the upper and lower terraces and a much higher density of aggregates. These properties are typical of hBN samples grown at all temperatures, though the differences are more pronounced as the growth temperature is increased. At higher growth temperature, figure 1(c), the hBN grows as hexagonal islands with very little aggregate formation at monolayer graphite steps. At the highest growth temperature, 1520 °C, figure 1(d), there is a near complete absence of boron nitride aggregate formation, but a much-reduced surface coverage of grown hBN layers. For each sample the width of the hBN monolayer growing from the HOPG edge is approximately constant across the surface, but the width varies with temperature, and, when varied, growth time.

Figure 2 highlights the dependence of the difference between growth from monolayer and multilayer HOPG steps on substrate temperature. Figures 2(a) and (b) were acquired using conductive AFM in which the topography in contact AFM mode (figure 2(a)), and the current flowing from a metal-coated cantilever (figure 2(b)) to the sample, are simultaneously measured. It can be difficult to distinguish a difference in topographic height between the growing hBN and the graphite step from which it nucleated (at least in the absence of additional aggregate formation), but there is clear contrast in the conductive AFM images (figure 2(b)) due to the pronounced difference in electrical properties of hBN and HOPG. Figure 2(a) shows a region of the surface, which includes growth from a monolayer HOPG step in the bottom and a bilayer HOPG step at the top of the image. Close to the monolayer HOPG step there is only a small topographic height variation between hBN and HOPG, but the difference in material is clear in the conductive image, in which the dark regions correspond to HOPG, which has higher conductivity, while the lighter regions correspond to hBN. This comparison shows the presence of a growing hBN terrace from a HOPG monolayer step and also illustrates that in this region there is less hBN growth on the upper as compared with the lower HOPG terrace. The bilayer HOPG step in the top of the figure has significant aggregate growth and there is less difference in growth of hBN on the upper and lower graphite terraces.

The trends apparent in these images are confirmed through a systematic analysis of the volume of aggregate material along HOPG edges identified as mono- or multistep. This can be extracted from the
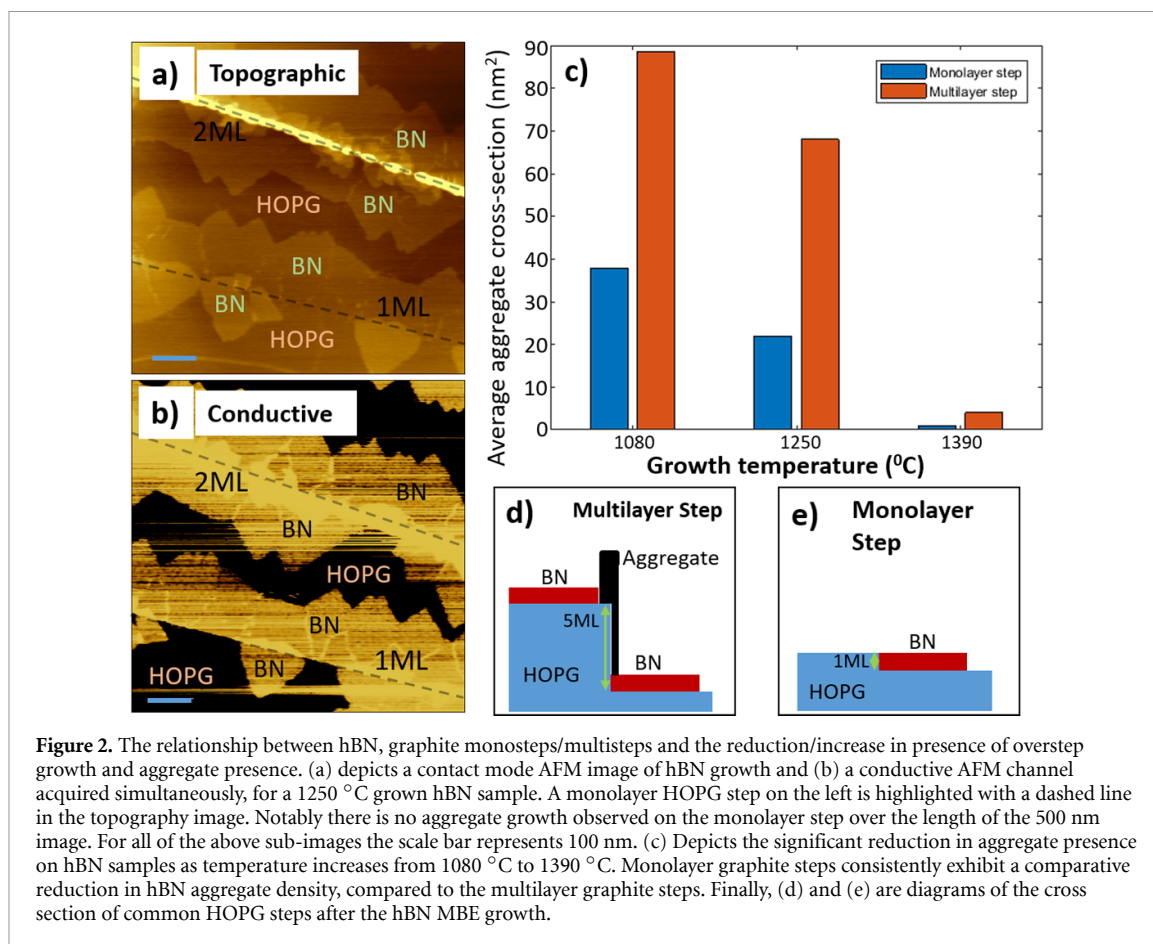
Figure 2. The relationship between hBN, graphite monosteps/multisteps and the reduction/increase in presence of overstep growth and aggregate presence. (a) depicts a contact mode AFM image of hBN growth and (b) a conductive AFM channel acquired simultaneously, for a 1250 °C grown hBN sample. A monolayer HOPG step on the left is highlighted with a dashed line in the topography image. Notably there is no aggregate growth observed on the monolayer step over the length of the 500 nm image. For all of the above sub-images the scale bar represents 100 nm. (c) Depicts the significant reduction in aggregate presence on hBN samples as temperature increases from 1080 °C to 1390 °C. Monolayer graphite steps consistently exhibit a comparative reduction in hBN aggregate density, compared to the multilayer graphite steps. Finally, (d) and (e) are diagrams of the cross section of common HOPG steps after the hBN MBE growth.

topographic images using Gwyddion's [59] 'flooding' tool and is then normalised by the length of the steps, leaving an area value which corresponds to the average cross-section of aggregates on each edge (five 5 μm square images have been analysed at each growth temperature). The results are summarised in the histogram shown in figure 2(c), which confirms that aggregate growth is lower at monolayer HOPG steps, and that, for all types of steps, reduces as substrate growth temperature is increased. The aggregated material should be minimised if clean interfaces are required, such as in the production of lateral or vertical heterostructures, and high growth temperatures provide a route to this objective. Figures 2(d) and (e) provide a schematic of the growth at multilayer and monolayer HOPG steps, respectively.

Figure 3 shows the influence of the growth temperature and time on the morphology and size of resulting hBN layers. Triangular and hexagonal hBN monolayer islands are revealed in (a) and (b). The alignment of the facet edges is determined from images of the islands with lattice resolution, which are shown in the insets and confirm that two different edge configurations, zigzag and armchair, are present, in, respectively, images (a) and (b). This assignment is consistent with the arguments of Liu *et al* [45] that hexagonal and triangular hBN islands or domains are associated with, respectively, armchair and zigzag

edges. As discussed in Liu *et al*, the expected hBN island edge selection depends on the chemical potential of the B and N constituents and thus the relative concentration of the B and N species on the surface during growth, which is additionally expected to depend on growth temperature [45, 60]. As is depicted in figures 1(a)–(d), we observed a general transition of the most prevalent hBN island edge from zigzag at lower substrate growth temperatures, to armchair at higher temperatures.

Figures 3(c) and (d) show the dependence of the width of the hBN layer on the growth time and substrate temperature, respectively. The width of the hBN sheet, as we define it here, is the average of the width of the hBN monolayer sheet over the length of an edge obtained by division of the area covered by the hBN sheet by the length of the edge. The results collated in (c) and (d) were taken from all edges on multiple 5 μm square images for each sample. At higher substrate temperatures a significant reduction in hBN width is observed. As a result, an optimum substrate growth temperature of ~1390 °C can be determined, which minimises aggregates (figure 2(c)), while retaining significant hBN layer formation. The average hBN monolayer coverage over the surface for a 40 min growth at 1390 °C is 10%. Higher hBN coverage can be obtained, while minimising aggregate density, by increasing the growth time. The growth
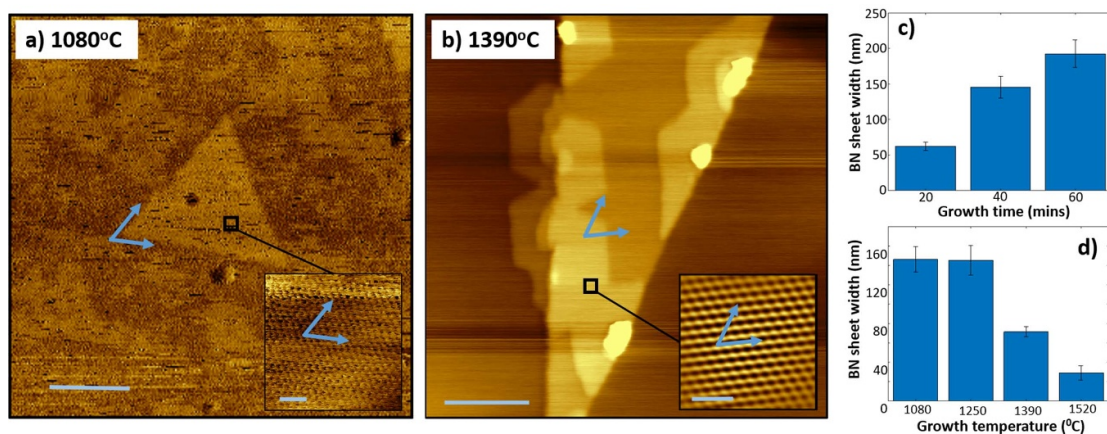
Figure 3. (a) and (b) show clear examples of hBN growth with different dominant facets. The scale bars are 200 nm (main images) and 1 nm (insets). The main images are contact-mode AFM topography images, whilst the insets are conductive channel images taken with a voltage of −50 mV. (a) Shows a zigzag edged island grown on a sample at 1080 °C. The higher temperature hBN sample, shown in (b), clearly depicts a hexagonal shape preference of the growth at 1390 °C. The insets are acquired over the smaller areas within the islands outlined by a black square; these images have lattice resolution allowing identification of the lattice directions, which are highlighted in blue and also overlaid on the islands in the larger scan. These show that the island facets are parallel (a) and approximately perpendicular (b) to the lattice vectors allowing identification of zigzag and armchair edges in, respectively, (a) and (b). (c) and (d) are bar charts showing how the hBN sheet widths varies with (c) growth time, with a constant substrate temperature of 1250 °C, and (d) growth temperature, with a constant growth time of 40 min.
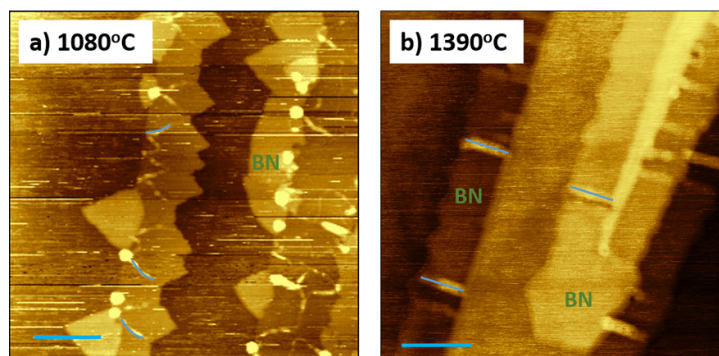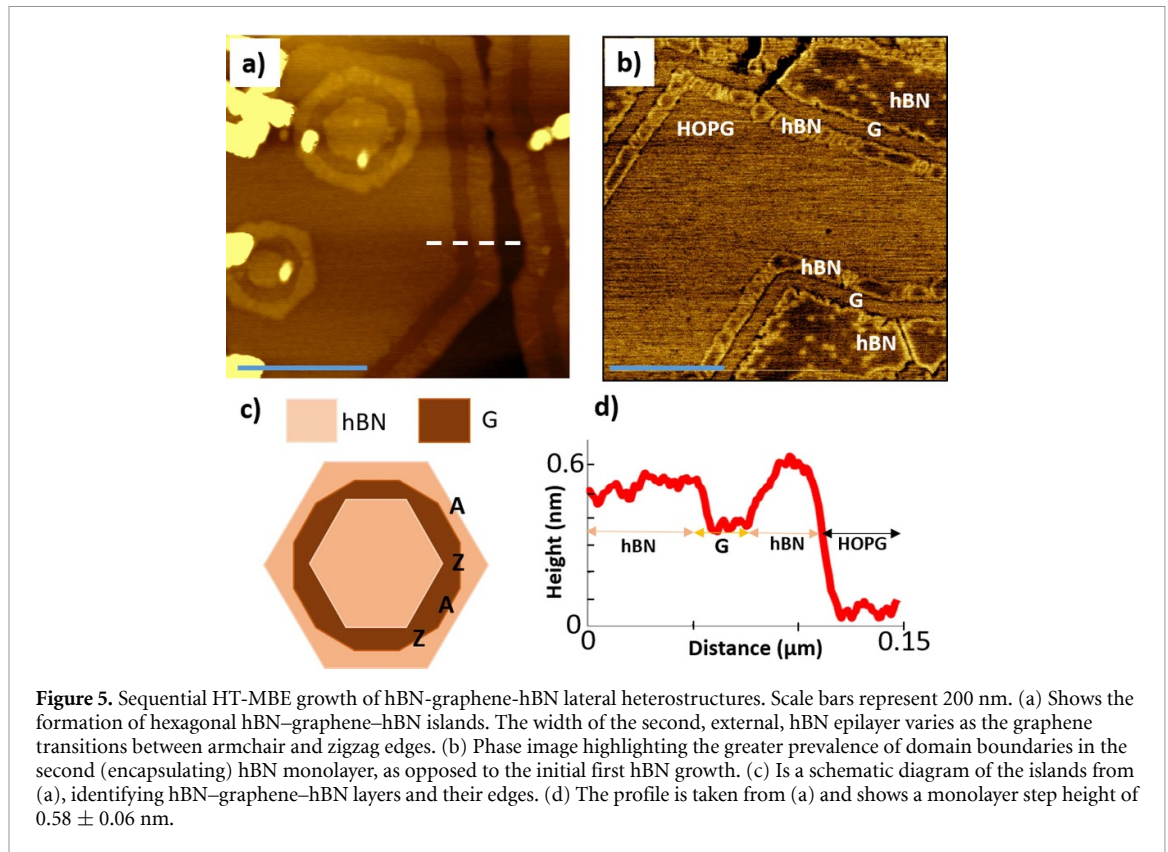

Figure 4. The variance in the grain boundaries formed during hBN growth, where two distinct types of boundary growth are observed. The scale bars are 200 nm (a) and 100 nm (b), respectively. (a) Shows boundaries that are curved, and not perpendicular to the HOPG/hBN interface. These curved hBN boundaries are commonly observed in the lower temperature samples. (b) Straight, hBN boundaries aligned perpendicular to the step edge are observed most commonly in the higher temperature samples.

of a second hBN monolayer is most commonly observed along highly aggregated HOPG multisteps, or from growth on hBN monolayer steps, as seen in figure 2(a). Thus, the loss of aggregates at higher temperatures would appear to reduce the available nucleation sites for a second monolayer, improving the viability of this method for the formation of single monolayer hBN applications.

In figure 4 we identify two distinct grain boundary regimes: (a) shows curved hBN grain boundaries that tend to merge as the growth progresses; (b) shows straight, hBN grain boundaries, parallel to the direction of growth. The grain boundaries are observed originating from the HOPG step edges and propagating alongside the hBN domains as they grow. These boundaries were observed in tapping mode AFM as raised tracks on the hBN monolayer sheet, or in conductive AFM as a reduction in conductivity. In

lower temperature grown hBN samples, such as that shown in figure 4(a), curved hBN external boundaries are identified. The domain boundaries are oriented at an angle to the direction of growth, which, if two boundaries meet, can lead to the enclosure of some domains as the growth proceeds. This may be caused by the mirroring of domains, originating from the dual component nature of hBN. If adjacent domains are mirrored (i.e. the positions of B and N atoms are reversed) they will not merge thus resulting in a boundary. At higher temperatures, as shown in figure 4(b), straight hBN island grain boundaries are observed aligned with the direction of growth, and thus perpendicular to the graphite step edge. As we established above, higher growth temperature results in hBN domains with armchair edges, as highlighted by the blue line in figure 4(b). These regions are therefore consistent with the growth of armchair

Figure 5. Sequential HT-MBE growth of hBN-graphene-hBN lateral heterostructures. Scale bars represent 200 nm. (a) Shows the formation of hexagonal hBN–graphene–hBN islands. The width of the second, external, hBN epilayer varies as the graphene transitions between armchair and zigzag edges. (b) Phase image highlighting the greater prevalence of domain boundaries in the second (encapsulating) hBN monolayer, as opposed to the initial first hBN growth. (c) Is a schematic diagram of the islands from (a), identifying hBN–graphene–hBN layers and their edges. (d) The profile is taken from (a) and shows a monolayer step height of 0.58 ± 0.06 nm.

terminated hBN islands from a zigzag terminated HOPG edge.

Figure 5 shows samples in which hBN, G and a final hBN epilayer have been sequentially grown by HT-MBE in two growth chambers without removal from the UHV system between cycles of growth. These are considered a crucial step to the formation of lateral hBN–G–hBN heterostructure devices. The images in figure 5 show a sample grown at 1390 °C, with an initial hBN growth time of 150 min, followed by a 1 min G growth, and encapsulated with a final hBN growth at 1390 °C for 10 min. The total sheet widths after three cycles of hBN–G–hBN monolayer growth on the surface of HOPG is 285 ± 10 nm. This is consistent with the widths obtained in figures 3(c) and (d), assuming the width is proportional to growth time.

In figure 5(a) two small hexagonal islands are observed on the surface of a larger hexagonal structure. The central hBN islands in the core of these small structures are bilayer regions of hBN formed in the first hBN growth cycle on a much larger monolayer hBN island. In subsequent cycles of growth, G, and then hBN, grows from the edges of these core hBN islands formed in the first growth cycle. In figure 5(a) the G strip appears as a slightly darker region and the second hBN forms the brighter area, which grows from the edge of the G. There are two different types of lateral heterostructures in figure 5(a). First, around the small initial core hexagonal hBN islands, the hBN-G-hBN lateral heterostructure is growing on the

surface of a hBN monolayer, formed in the first cycle of growth. At the same time, the second hBN–G–hBN lateral heterostructure, with similar, but not identical, dimensions is growing from the edge of a large hBN monolayer directly on the surface of HOPG substrate.

Figure 5 highlights the conformal nature of the lateral heterostructure. In figure 5(a) the shape of the first hBN layer is clearly hexagonal, as expected for this HT-MBE growth temperature, with each hBN edge following the armchair direction. The G layer initially grows with an armchair edge, following the first layer hBN monolayer edge direction, but undergoes a transition to zigzag edge close to the vertices of the inner hBN hexagon, similar to previous observations by Thomas *et al* [35]. Figures 5 (a) and (b) show the near-uniform width of the G epilayer, the width only changing significantly close to hBN vertices. Excluding these regions, the average G epilayer width is 25 ± 2 nm for the regions growing on HOPG, and 23 ± 2 nm growing around the hexagonal bilayer hBN islands. As can be seen in figure 5(a) the width of hBN growing in the second cycle is 34 ± 1 nm on the HOPG substrate, but 20 ± 1 nm around the hBN islands. This implies the growth rate of the encapsulating hBN sheet is higher when grown on HOPG as compared with the regions grown on the surface of the monolayer hBN revealing a substrate dependence of the HT-MBE growth of hBN. Finally, figure 5(d) shows profiles from which the widths of the outer two epilayers are determined, alongside a small height difference observed

between the G and hBN monolayers in our contact AFM images (an apparent height difference can arise due to material-dependent probe–surface interactions and differences in material properties such as elastic constant, frictional coefficient etc, which result in small, cantilever-dependent variations in the equilibrium tip position under the constant force conditions used in contact mode AFM). This has been also observed by other research groups [61, 62]). Overall, figure 5 demonstrates that highly uniform G monolayers have been grown conformally from a nucleating hBN monolayer and can subsequently be encapsulated by a second hBN strip to form a hBN–G–hBN lateral heterostructure.

Lateral hBN–G–hBN heterostructures grown by the developed HT-MBE method have abrupt hetero interfaces between hBN and G monolayers and good width uniformity, as shown in figure 5. The abruptness of these interfaces and width uniformity are similar or even better, than in lateral structures obtained by CVD growth techniques, for example, demonstrated recently by sequential CVD growth of G–hBN–G [63] or G–hBN [64, 65] lateral heterostructures.

4. Conclusions

In conclusion, we have studied the HT-MBE epitaxy of hBN monolayers on a graphite HOPG substrates. It has been shown that the HT-MBE growth can be tuned by substrate growth temperature to minimise BN aggregates formation on the hBN surface, and to alter the preferred edge of the hBN monolayer grain sheet. Monolayer thick hBN, grown at a higher temperature, exhibited armchair edges, minimal aggregate presence, and a reduced but significant width of the hBN monolayer sheet. The growth temperature of 1390 °C is identified as the temperature of choice for HT-MBE for reducing aggregates while retaining the quality of hBN layers. Subsequent HT-MBE epitaxy of hBN, G and hBN monolayers demonstrate a capability for the growth of lateral hBN–G–hBN heterostructures with edges structure control.

The hBN–G interface of the monolayer thick lateral heterostructure defines their resulting electronic and magnetic properties. Therefore, our future HT-MBE studies will concentrate on the exploration of growth parameters to improve the quality of these monolayer thick hBN–G lateral heterointerfaces.

Data availability statement

The image files on which the figures in this paper are based are available at doi https://doi.org/10.17639/nott.7100

ORCID iDs

Jonathan Bradford ⬤ https://orcid.org/0000-0003-2356-5816
Sergei V Novikov ⬤ https://orcid.org/0000-0002-3725-2565
Peter H Beton ⬤ https://orcid.org/0000-0002-2120-8033

References

[1] Caldwell J D, Aharonovich I, Cassabois G, Edgar J H, Gil B and Basov D N 2019 Photonics with hexagonal boron nitride *Nat. Rev. Mater.* **4** 552–67
[2] Watanabe K, Taniguchi T and Kanda H 2004 Direct-bandgap properties and evidence for ultraviolet lasing of hexagonal boron nitride single crystal *Nat. Mater.* **3** 404–9
[3] Cassabois G, Valvin P and Gil B 2016 Hexagonal boron nitride is an indirect bandgap semiconductor *Nat. Photon.* **10** 262–6
[4] Tran T T, Bray K, Ford M J, Toth M and Aharonovich I 2016 Quantum emission from hexagonal boron nitride monolayers *Nat. Nanotechnol.* **11** 37–41
[5] Geim A K and Grigorieva I V 2013 van der Waals heterostructures *Nature* **499** 419–25
[6] Yankowitz M, Xue J and LeRoy B J 2014 Graphene on hexagonal boron nitride *J. Phys.: Condens. Matter* **26** 303201
[7] Elias C *et al* 2019 Direct band-gap crossover in epitaxial monolayer boron nitride *Nat. Commun.* **10** 2639
[8] Han X, Lin J, Liu J, Wang N and Pan D 2019 Effects of hexagonal boron nitride encapsulation on the electronic structure of few-layer MoS_2 *J. Phys. Chem. C* **123** 14797–802
[9] Kim K K, Lee H S and Lee Y H 2018 Synthesis of hexagonal boron nitride heterostructures for 2D van der Waals electronics *Chem. Soc. Rev.* **47** 6342–69
[10] Khan M H, Liu H K, Sun X, Yamauchi Y, Bando Y, Golberg D and Huang Z 2017 Few-atomic-layered hexagonal boron nitride: CVD growth, characterization, and applications *Mater. Today* **20** 611–28
[11] Auwärter W 2019 Hexagonal boron nitride monolayers on metal supports: versatile templates for atoms, molecules and nanostructures *Surf. Sci. Rep.* **74** 1–95
[12] Song X *et al* 2015 Chemical vapor deposition growth of large-scale hexagonal boron nitride with controllable orientation *Nano Res.* **8** 3164–76
[13] Jeong H, Kim D Y, Kim J, Moon S, Han N, Lee S H, Okello O F N, Song K, Choi S-Y and Kim J K 2019 Wafer-scale and selective-area growth of high-quality hexagonal boron nitride on Ni(111) by metal-organic chemical vapor deposition *Sci. Rep.* **9** 5736
[14] Chang R J, Wang X, Wang S, Sheng Y, Porter B, Bhaskaran H and Warner J H 2017 Growth of large single-crystalline monolayer hexagonal boron nitride by oxide-assisted chemical vapor deposition *Chem. Mater.* **29** 6252–60

[15] Ji Y, Calderon B, Han Y, Cueva P, Jungwirth N R, Alsalman H A, Hwang J, Fuchs G D, Muller D A and Spencer M G 2017 Chemical vapor deposition growth of large single-crystal Mono-, Bi-, tri-layer hexagonal boron nitride and their interlayer stacking *ACS Nano* **11** 12057–66

[16] Lee J S *et al* 2018 Wafer-scale single-crystal hexagonal boron nitride film via self-collimated grain formation *Science* **362** 817–21

[17] Wu Q, Lee J, Sun J and Song Y J 2018 *In situ* direct growth of graphene/hexagonal boron nitride heterostructure on SiO₂ substrate without metal catalyst *Carbon* **138** 76–80

[18] Jiang H X and Lin J Y 2017 Review—hexagonal boron nitride epilayers: growth, optical properties and device applications *ECS J. Solid State Sci. Technol.* **6** Q3012–21

[19] Shim J *et al* 2018 Controlled crack propagation for atomic precision handling of wafer-scale two-dimensional materials *Science* **362** 665–70

[20] Rice A, Allerman A, Crawford M, Beechem T, Ohta T, Spataru C, Figiel J and Smith M 2018 Effects of deposition temperature and ammonia flow on metal-organic chemical vapor deposition of hexagonal boron nitride *J. Cryst. Growth* **485** 90–95

[21] Glavin N R, Chabak K D, Heller E R, Moore E A, Prusnick T A, Maruyama B, Walker D E, Dorsey D L, Paduano Q and Snure M 2017 Flexible gallium nitride for high-performance, strainable radio-frequency devices *Adv. Mater.* **29** 1701838

[22] Gannett W, Regan W, Watanabe K, Taniguchi T, Crommie M F and Zettl A 2011 Boron nitride substrates for high mobility chemical vapor deposited graphene *Appl. Phys. Lett.* **98** 242105

[23] Hirama K, Taniyasu Y, Karimoto S, Krockenberger Y and Yamamoto H 2014 Single-crystal cubic boron nitride thin films grown by ion-beam-assisted molecular beam epitaxy *Appl. Phys. Lett.* **104** 092113

[24] Hirama K, Taniyasu Y, Karimoto S, Yamamoto H and Kumakura K 2017 Heteroepitaxial growth of single-domain cubic boron nitride films by ion-beam-assisted MBE *Appl. Phys. Express* **10** 035501

[25] Tsai C L, Kobayashi Y, Akasaka T and Kasu M 2009 Molecular beam epitaxial growth of hexagonal boron nitride on Ni(1 1 1) substrate *J. Cryst. Growth* **311** 3054–7

[26] Nakhaie S, Wofford J M, Schumann T, Jahn U, Ramsteiner M, Hanke M, Lopes J M J and Riechert H 2015 Synthesis of atomically thin hexagonal boron nitride films on nickel foils by molecular beam epitaxy *Appl. Phys. Lett.* **106** 213108

[27] Tonkikh A A, Voloshina E N, Werner P, Blumtritt H, Senkovskiy B, Güntherodt G, Parkin S S P and Dedkov Y S 2016 Structural and electronic properties of epitaxial multilayer h-BN on Ni(111) for spintronics applications *Sci. Rep.* **6** 23547

[28] Wofford J M, Nakhaie S, Krause T, Liu X, Ramsteiner M, Hanke M, Riechert H and Lopes J J M 2017 A hybrid MBE-based growth method for large-area synthesis of stacked hexagonal boron nitride/graphene heterostructures *Sci. Rep.* **7** 43644

[29] Xu Z, Zheng R, Khanaki A, Zuo Z and Liu J 2015 Direct growth of graphene on *in situ* epitaxial hexagonal boron nitride flakes by plasma-assisted molecular beam epitaxy *Appl. Phys. Lett.* **107** 213103

[30] Xu Z, Khanaki A, Tian H, Zheng R, Suja M, Zheng J G and Liu J 2016 Direct growth of hexagonal boron nitride/graphene heterostructures on cobalt foil substrates by plasma-assisted molecular beam epitaxy *Appl. Phys. Lett.* **109** 043110

[31] Xu Z, Tian H, Khanaki A, Zheng R, Suja M and Liu J 2017 Large-area growth of multi-layer hexagonal boron nitride on polished cobalt foils by plasma-assisted molecular beam epitaxy *Sci. Rep.* **7** 43100

[32] Gupta V K, Wamsley C C, Koch M W and Wicks G W 1999 Molecular beam epitaxy growth of boron-containing nitrides *J. Vac. Sci. Technol.* B **17** 1246

[33] Cheng T, Summerfield A, Mellor C, Khlobystov A, Eaves L, Foxon C, Beton P and Novikov S 2018 High-temperature molecular beam epitaxy of hexagonal boron nitride with high active nitrogen fluxes *Materials* **11** 1119

[34] Cho Y-J *et al* 2016 Hexagonal boron nitride tunnel barriers grown on graphite by high temperature molecular beam epitaxy *Sci. Rep.* **6** 34474

[35] Thomas J *et al* 2020 Step-flow growth of graphene-boron nitride lateral heterostructures by molecular beam epitaxy *2D Mater.* **7** 035014

[36] Cheng T S, Summerfield A, Mellor C J, Davies A, Khlobystov A N, Eaves L, Foxon C T, Beton P H and Novikov S V 2018 High-temperature molecular beam epitaxy of hexagonal boron nitride layers *J. Vac. Sci. Technol.* B **36** 02D103

[37] Wang J, Li Z, Chen H, Deng G and Niu X 2019 Recent advances in 2D lateral heterostructures *Nano-Micro Lett.* **11** 48

[38] Wang H, Liu F, Fu W, Fang Z, Zhou W and Liu Z 2014 Two-dimensional heterostructures: fabrication, characterization, and application *Nanoscale* **6** 12250–72

[39] Zhang J, Xie W, Zhao J and Zhang S 2016 Band alignment of two-dimensional lateral heterostructures *2D Mater.* **4** 015038

[40] Zhang D, Zhang D-B, Yang F, Lin H-Q, Xu H and Chang K 2015 Interface engineering of electronic properties of graphene/boron nitride lateral heterostructures *2D Mater.* **2** 041001

[41] Özçelik V O, Durgun E and Ciraci S 2015 Modulation of electronic properties in laterally and commensurately repeating graphene and boron nitride composite nanostructures *J. Phys. Chem.* C **119** 13248–56

[42] Ge M and Si C 2018 Mechanical and electronic properties of lateral graphene and hexagonal boron nitride heterostructures *Carbon* **136** 286–91

[43] Li Q, Liu M, Zhang Y and Liu Z 2016 Hexagonal boron nitride–graphene heterostructures: synthesis and interfacial properties *Small* **12** 32–50

[44] Ci L *et al* 2010 Atomic layers of hybridized boron nitride and graphene domains *Nat. Mater.* **9** 430–5

[45] Liu Y, Bhowmick S and Yakobson B I 2011 BN white graphene with 'colorful' edges: the energies and morphology *Nano Lett.* **11** 3113–6

[46] Bhowmick S, Singh A K and Yakobson B I 2011 Quantum dots and nanoroads of graphene embedded in hexagonal boron nitride *J. Phys. Chem.* C **115** 9889–93

[47] Drost R, Uppstu A, Schulz F, Hämäläinen S K, Ervasti M, Harju A and Liljeroth P 2014 Electronic states at the graphene–hexagonal boron nitride zigzag interface *Nano Lett.* **14** 5128–32

[48] Liu Z, Song L, Zhao S, Huang J, Ma L, Zhang J, Lou J and Ajayan P M 2011 Direct growth of graphene/hexagonal boron nitride stacked layers *Nano Lett.* **11** 2032–7

[49] Liu L, Park J, Siegel D A, McCarty K F, Clark K W, Deng W, Basile L, Idrobo J C, Li A-P and Gu G 2014 Heteroepitaxial growth of two-dimensional hexagonal boron nitride templated by graphene edges *Science* **343** 163–7

[50] Sutter P, Huang Y and Sutter E 2014 Nanoscale integration of two-dimensional materials by lateral heteroepitaxy *Nano Lett.* **14** 4846–51

[51] Lu J, Zhang K, Feng Liu X, Zhang H, Chien Sum T, Castro Neto A H and Loh K P 2013 Order–disorder transition in a two-dimensional boron–carbon–nitride alloy *Nat. Commun.* **4** 2681

[52] Gao Y *et al* 2013 Toward single-layer uniform hexagonal boron nitride–graphene patchworks with zigzag linking edges *Nano Lett.* **13** 3439–43

[53] Camilli L, Jørgensen J H, Tersoff J, Stoot A C, Balog R, Cassidy A, Sadowski J T, Bøggild P and Hornekær L 2017 Self-assembly of ordered graphene nanodot arrays *Nat. Commun.* **8** 47

[54] Liu Z *et al* 2013 In-plane heterostructures of graphene and hexagonal boron nitride with controlled domain sizes *Nat. Nanotechnol.* **8** 119–24

[55] Levendorf M P, Kim C J, Brown L, Huang P Y, Havener R W, Muller D A and Park J 2012 Graphene and boron nitride lateral heterostructures for atomically thin circuitry *Nature* **488** 627–32

[56] Wang H S *et al* 2021 Towards chirality control of graphene nanoribbons embedded in hexagonal boron nitride *Nat. Mater.* **20** 202–7

[57] Summerfield A *et al* 2016 Strain-engineered graphene grown on hexagonal boron nitride by molecular beam epitaxy *Sci. Rep.* **6** 22440

[58] Davies A *et al* 2018 Lattice-matched epitaxial graphene grown on boron nitride *Nano Lett.* **18** 498–504

[59] Nečas D and Klapetek P 2012 Gwyddion: an open-source software for SPM data analysis *Cent. Eur. J. Phys.* **10** 181–8

[60] Zhang Z, Liu Y, Yang Y and Yakobson B I 2016 Growth mechanism and morphology of hexagonal boron nitride *Nano Lett.* **16** 1398–403

[61] Fernandes T F D and Neves B R A 2016 Friction coefficient mapping of 2D materials via friction-induced topographic artifact in atomic force microscopy *J. Adv. Nanomater.* **1** 73–81

[62] Shearer C J, Slattery A D, Stapleton A J, Shapter J G and Gibson C T 2016 Accurate thickness measurement of graphene *Nanotechnology* **27** 125704

[63] Makino R, Mizuno S, Kageshima H and Hibino H 2020 Controlled CVD growth of lateral and vertical graphene/h-BN heterostructures *Appl. Phys. Express* **13** 065007

[64] Wei W, Pan J, Euaruksakul C, Yang Y, Cui Y, Fu Q and Bao X 2020 Dynamic observation of in-plane h-BN/graphene heterostructures growth on Ni(111) *Nano Res.* **13** 1789–94

[65] Geng D, Dong J, Kee A L, Ding F and Yang H Y 2019 *In situ* epitaxial engineering of graphene and h-BN lateral heterostructure with a tunable morphology comprising h-BN domains *NPG Asia Mater.* **11** 56